Remote Sensing of Environment 331 (2025) 115031

Contents lists available at ScienceDirect

Remote Sensing of Environment

journal homepage: www.elsevier.com/locate/rse

Segmenting and characterising ripple patterns on sand dunes using machine learning and 2D semi-variogram

Lucie A. Delobel [a,*], David Moffat [b], Emma Tebbs [a], Andreas C.W. Baas [a]

[a] *Department of Geography, School of Social Science and Public Policy, King's College London, London, United Kingdom*
[b] *Earth Observation Science and Applications, Plymouth Marine Laboratory, Plymouth, United Kingdom*

ARTICLE INFO

Edited by Jing M. Chen

Keywords:
Texture segmentation
U-net model
Spatial autocorrelation
HiRISE
Mars

ABSTRACT

Sand ripples, shaped by fluid flow like wind or water, are common on dunes on Earth and Mars. Their patterns reveal local transport conditions, offering insights into wind regimes where direct observations are lacking. Since manual mapping is slow and subjective, automated methods are essential for consistent large-scale analysis. This study presents two novel and complementary methods for mapping ripple patterns on Martian dunes using high-resolution imagery: a U-Net model for pattern classification and a 2D semi-variogram for measuring ripple spacing and orientation. Tested on 42 barchan dunes across six Martian regions, the U-Net showed reliable ripple classification (F1-score 79 %), while the variogram method achieved high accuracy for ripple spacing ($R^2 = 0.78$) and orientation ($R^2 = 0.98$). Together, these approaches enable efficient, large-scale analysis of ripples for sediment transport on any planetary surface and can be applied to other patterned features.

1. Introduction

When sedimentary surfaces composed of granular materials, such as sand, are exposed to sufficiently strong fluid flow (e.g., air or water), they develop ripples of varying sizes and patterns. On Earth, wind is responsible for aeolian sand transport and creating impact ripples with wavelengths of up to 24 cm and typically displaying a 2D morphology with straight, symmetrical crests (Pye and Tsoar, 2009; Rubin, 2012; Sharp, 1963). In subaqueous settings, waves and water currents form fluid drag ripples with similar wavelengths to impact ripples but exhibiting a range of shapes - from straight to asymmetrical forms such as sinuous or 3D morphologies - depending on factors like the flow velocity and the height above the seafloor (Allen, 1963; Wynn et al., 2002). Both types of ripples can be found superimposed on larger bedforms and numerous studies in the past have analysed ripple patterns to determine the fluid flow that shaped them (Allen, 1963; Tanner, 1967). Ripples have also been observed on the surface of Mars, and there is ongoing debate about whether they are formed by grain impact or fluid drag processes (Lorenz, 2020; Lapotre et al., 2021; Yizhaq et al., 2024). Given their widespread presence and their reflection of local surface flows, ripples can serve as a valuable reference in areas where in situ observations of fluid flow are lacking, such as on Mars (Jackson et al., 2015; Hood et al., 2021), or to describe past flow environments from the sedimentary records (Vaz et al., 2023).

Determining local fluid flow requires mapping the ripples, but manual methods are time-consuming and subjective. As a result, in the last two decades, numerous researchers have explored different techniques, from mathematical analyses to machine learning, to automatically identify dunes or ripples on Earth and Mars. Earlier studies primarily focused on signal processing methods such as spatial cross-correlation (Duffy and Hughes-Clarke, 2005), Wavelet Transform (Cataño-Lopera et al., 2009), variogram (Robert and Richards, 1988; van Dijk et al., 2008), Fourier Transform (Cazenave et al., 2013; Vaz et al., 2023), Radon Transform (Gadhiraju et al., 2014) and neighbourhood analysis (Lebrec et al., 2022), or fingerprint algorithms (Skarke and Trembanis, 2011) to extract bedform features such as their crest, outline, or orientation. More recently, supervised machine learning models such as Random Forest and Object Based Image Analysis (OBIA) from the computer vision field have gained popularity for mapping dunes and ripples based on their spectral and spatial properties (Cardinale et al., 2020; Zheng et al., 2020; Zheng et al., 2024a). Occasionally, OBIA is combined with Artificial Neural Networks (ANN) to improve either the segmentation or the classification of the bedforms in images (Silvestro et al., 2016). Over the last 7 years, Convolutional Neural Networks (CNN), a subset of ANN, have been extensively applied for mapping large bedforms (Rubanenko et al., 2021; Tang et al., 2023;

---

* Corresponding author.
E-mail address: lucie.delobel@kcl.ac.uk (L.A. Delobel).

https://doi.org/10.1016/j.rse.2025.115031
Received 14 January 2025; Received in revised form 12 September 2025; Accepted 14 September 2025

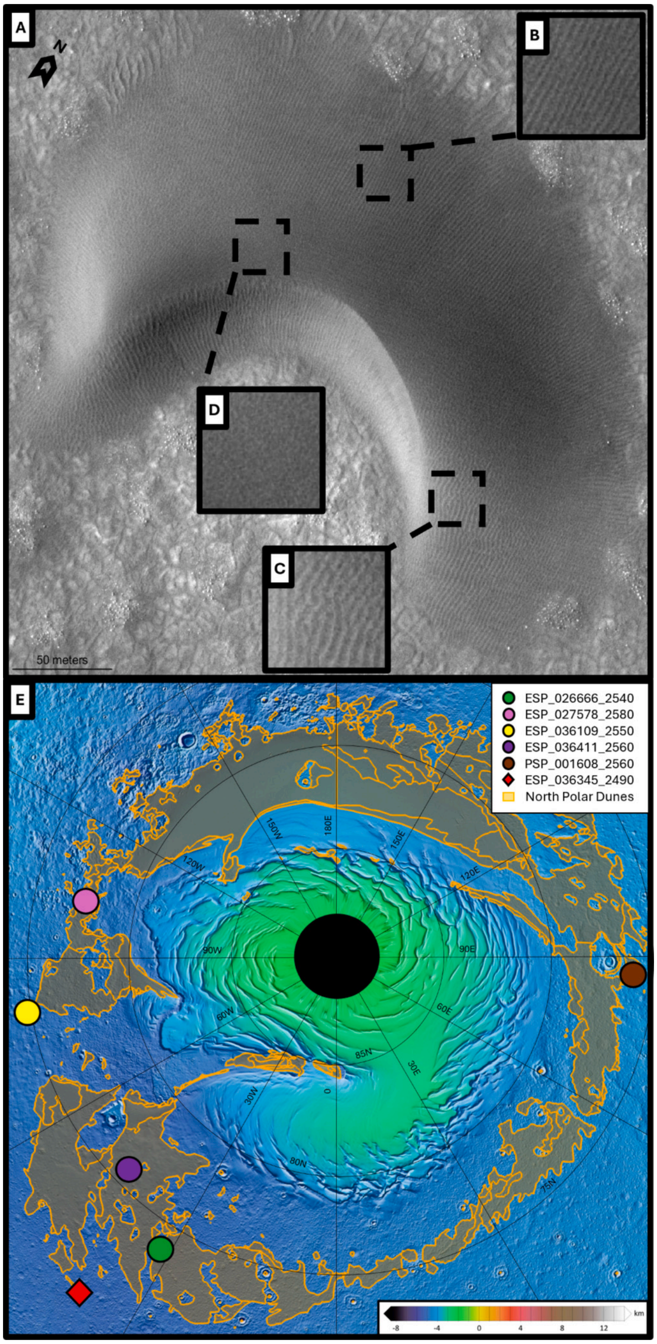

Fig. 1. (A) A barchan dune superimposed with ripples displaying a variety of patterns from HiRISE image ESP_036411_2560. (B) A zoom-in tile of straight ripples, (C) sinuous ripples, and (D) complex textures. (E) The six HiRISE images selected for this study are located within the north polar dune field of Mars. The images set aside for training are represented by circles, and the one for testing by a red diamond. The base map is Mars Orbiter Laser Altimeter (MOLA) shaded relief with colourised elevation. (For interpretation of the references to colour in this figure legend, the reader is referred to the web version of this article.)

Zheng et al., 2024b) due to their ability to minimise pre-processing requirements. Few studies have employed unsupervised models for digitising and clustering large bedforms, such as K-Means clustering in combination with principal component analysis (Vaz et al., 2017).

Most of these approaches focused on extracting bedform features, such as their crestline, outline or orientation, to derive further characteristics about the morphology (e.g., wavelength, asymmetry, crest defects) and dynamics (e.g., migration rates and direction) of the bedforms or to identify the bedform type. Therefore, the techniques developed in these studies are primarily focused on bedforms and are not directly applicable to other fields. A more flexible method that emphasises mapping patterns, or 'textures,' instead of specific traits of individual bedforms could potentially extend its applicability to other features, such as vegetation patterns (Tarnita, 2024; Rietkerk et al., 2021). However, research on texture segmentation in aeolian studies has been limited. Only four studies have classified patterns of dunes based on spatial orientation (Gadhiraju et al., 2014), the morphology of the dune and inter-dune areas (Tang et al., 2023), and spatial arrangements (Zheng et al., 2024b; Zheng et al., 2020). Additionally, only two studies have segmented ripple patterns into two-dimensional (long and regular crests) or three-dimensional (shorter and irregular crests) categories based on their degree of straightness, using the horizontal form index (Silvestro et al., 2016; Vaz et al., 2017). This index corresponds to the ratio of ripple length to wavelength (Allen, 1968). Furthermore, these studies were conducted over a range of bedforms and for only two specific sites.

Our study quantifies ripple patterns and maps their distribution across barchan dunes in remote sensing imagery. Three types of patterns are identified for classification: straight ripples, sinuous ripples, and complex textures. Two texture segmentation techniques were applied to classify the ripple patterns based on training tiles: (1) a spatial autocorrelation analysis known as a 2D semi-variogram, and (2) a supervised machine learning model called U-Net, which is a type of CNN. The performance of both methods was evaluated for several input tile sizes and overlap sizes. In addition, we investigated the use of the 2D semi-variogram to measure ripple spacing and orientation. While this study focused on Mars due to the availability of free high-resolution satellite imagery of ripples over barchan dunes, both texture segmentation approaches can be adapted for use with Unmanned Aerial Vehicle imagery of terrestrial aeolian bedforms, bathymetric data of subaqueous bedforms, or for other fields of study such as spatial ecology for vegetation patterns.

2. Study area and data

Sand transport by wind is the dominant force shaping the contemporary surface of Mars, yet our knowledge of these processes is still limited. Three-quarters of the dune fields are located in the northern polar region, between 70°N and 90°N latitudes (Hayward et al., 2014). Furthermore, two-thirds of Mars' north polar dune field is covered by barchan dunes (Rubanenko et al., 2021), crescent-shaped dunes which are formed by unidirectional winds with limited sand supply (Wasson and Hyde, 1983), making them an ideal case study for mapping the superimposing ripples.

Despite the differences between the planets' aeolian environments, Mars bedforms have striking similarities with those on Earth (Hayward et al., 2014; Sherman et al., 2024). Since the deployment of the Mars Reconnaissance Orbiter in 2006, the High Resolution Imaging Science Experiment (HiRISE) camera has been capturing ripples over Martian dunes that have wavelengths on the order of meters and display a variety of patterns. In Fig. 1A, straight ripples are found along the edges and stoss slope of the dune (Fig. 1B), whereas some sinuous textures are located on the right horn (Fig. 1C). Close to the dune's crest, the pattern is indistinct (Fig. 1D), which could be due to the ripple wavelength being smaller than the image resolution or resulting from a complex wind regime, such as inconsistent wind directions preventing the formation of well-structured ripples. In terrestrial aeolian settings, straight ripples are generally the most common (Tanner, 1967; Rubin, 2012) and sinuosity is likely caused by a grain size differentiation between the crests and troughs. In subaqueous settings, ripples range in morphology from straight, sinuous, catenary, to linguoid, and lunate (Allen, 1963). Sinuosity is linked to increased flow velocity, height above the seafloor, and whether the ripples were formed by waves or currents (Reineck and

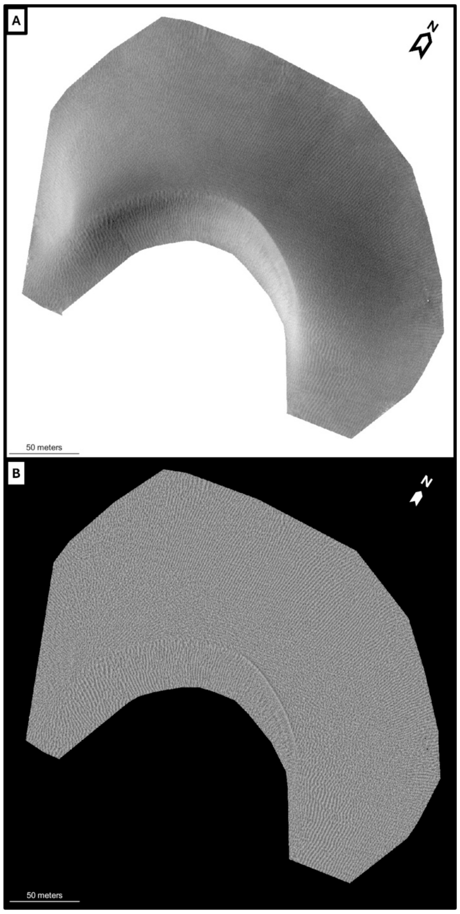

Fig. 2. (A) An isolated barchan dune from the HiRISE image ESP_036411_2560 with the illumination differences and (B) the same dune after pre-processing.

Singh, 1980; Wynn et al., 2002).

For this study, six HiRISE image sites with a resolution of 0.25 m/pixel were selected (Table S1), each image covering on average 157.5 km^2 (McEwen et al., 2007). These sites feature at least a dozen individual barchan dunes with ripples and are located in the highly active sand transport area of the northern polar region, outside of craters with complex wind patterns (Fig. 1E). Although some HiRISE sites have associated Digital Terrain Models (DTMs), these DTMs do not capture the elevation of the ripple topography (Vaz et al., 2017); thus, we are restricted to using HiRISE imagery for our analysis. We downloaded the highest quality red band image (550 to 850 nm wavelength, McEwen et al., 2007) for each location, ensuring that the ripples were clearly distinguishable and not obscured by poor illumination or dust cover. Using QGIS (Long Term Release 3.34), we manually outlined and cropped isolated barchan dunes from the HiRISE images. This process resulted in two TIF versions for each dune: one cropped version, as displayed in Fig. 1A, and a second version in which any areas outside the dune outline—specifically, the surrounding bedrock—are masked. This masking was achieved using the Geographic Resources Analysis Support System (GRASS) toolbox in QGIS. 45 dunes from five of the selected HiRISE images (Fig. 1E, circles) were assigned to the training dataset (83 %), and nine dunes from the last HiRISE image (Fig. 1E, red diamond) to the testing dataset (17 %, Table S1).

3. Methodology

3.1. Research strategy

The overall processing sequence was as follows: barchan dunes in the HiRISE images were isolated and processed to improve the visibility of the superimposing ripples (Section 3.2). Subsequent analysis involved classifying three ripple textures: straight ripples, sinuous ripples, and complex textures (Section 3.3). This process occurred in two stages. First, tiles of different sizes were created to represent the various textures and were used to train and test two texture segmentation techniques: (1) a machine learning model (Section 3.4) and (2) a 2D semi-variogram method (Section 3.5). In the second stage, both techniques were applied to entire dunes by analysing sliding windows with varying overlaps to produce texture maps. The performance of both segmentation techniques and the impact of tile and overlap size were statistically evaluated against observations (Section 3.6). Finally, to characterise the textures, the ripple spacing and orientation were calculated with the 2D semi-variogram and assessed against manual measurements (Section 3.5).

3.2. Preprocessing of HiRISE dune imagery

A crucial step in the processing was to remove illumination differences. Due to the grayscale nature of the HiRISE images, ripple patterns on the sunlit side of the dune were less visible due to the lower contrast between the ripple crests and troughs. Furthermore, illumination differences may mislead segmentation methods in classifying images based on both texture and average intensity of the regions (i.e., sunlit vs shadows) (Karabağ et al., 2019). To equalise and standardise the ripple contrast in the cropped TIF, a circular 2D filter with a width of 15 pixels was applied and divided by the local Root Mean Square to ensure there were no spatial variations in the intensity range between the ripple crests and troughs (or any other topography). Hence, the standardised images are more uniform, and the only differences have to do with the ripple textures.

The optimal filter width was determined by applying a range of filter sizes (3 to 29 pixels) on several test sections from a dozen dunes from different images. We extracted the ripples by removing the filtered image from the original image and then selected the filter width producing the highest standard deviation value of the extracted ripples. While there were some slight variations in the optimal filter width among different sections of a dune and between dunes, on average, a filter width of 15 pixels produced the best results.

Finally, the surrounding bedrock and any remaining rock within the dune surface were removed, as these elements have a higher pixel intensity than the surrounding dark sand. The surrounding bedrock was masked (NaN values) in the standardised image by overlaying the TIF of the dune outline (see Section 2). In some cases, individual rocks were identified within the dunes as bright patches that interrupt the ripple pattern (e.g., the two white dots near the right edge of the dune in Fig. 2A) and were manually cropped out (Fig. S1). The resulting images display a variety of ripple patterns and textures across the dune's surface (Fig. 2B).

3.3. Creating labelled tiles for different ripple types

After visually inspecting over 50 processed dune images, we identified three common types of textures: straight ripples (Fig. 1B), sinuous ripples (Fig. 1C), and complex textures (Fig. 1D). Following the classifications from previous studies (Silvestro et al., 2016; Vaz et al., 2017; Hood et al., 2021), straight ripples are characterised as two-dimensional bedforms exhibiting elongated and uniform crests, whereas sinuous ripples correspond to three-dimensional forms with shorter and irregular crests. A third category, termed complex textures, encompasses surfaces lacking discernible ripple patterns.

Subset images were manually extracted from 31 dunes in the training dataset, ensuring that each image clearly displayed one of the ripple pattern types. Samples were taken from various areas of the dunes, including flanks, horns, and stoss slope. For each texture, 20 labelled tiles were created. This resulted in a total of 60 labelled tiles for each of

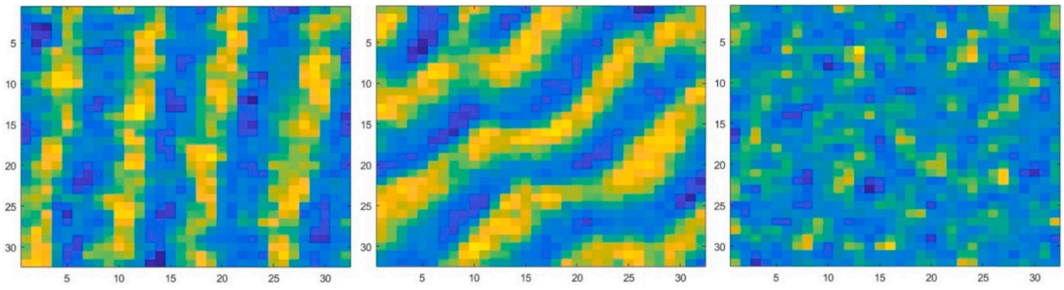

Fig. 3. Examples of 32 × 32 pixels labelled tiles for straight (left) and sinuous ripples (centre), and complex textures (right).

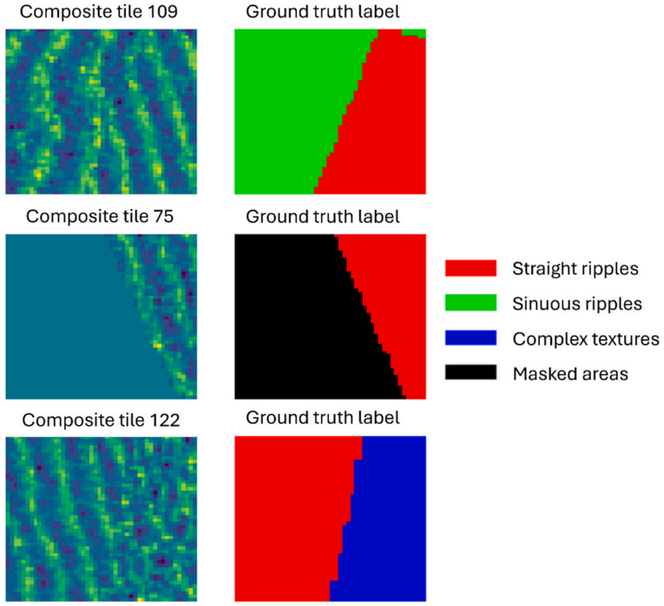

Fig. 4. Sample of composite tiles (left column) with their respective ground truth label (right column).

three tile sizes: 32 × 32, 48 × 48 and 64 × 64 pixels (Fig. 3). The rationale for selecting three tile sizes was to assess whether the segmentation approaches would recognise textures better for larger or smaller tile sizes, an approach already tested by Gadhiraju et al. (2014). Larger tile sizes might encompass more than one ripple pattern, while too small of a tile size might not capture enough texture information to determine a pattern. To evaluate the performance of the two texture segmentation methods on selecting the best tile size, an independent set of labelled tiles was created from the testing dataset. This time, however, only five tiles per ripple type were generated for the three tile sizes from nine dunes.

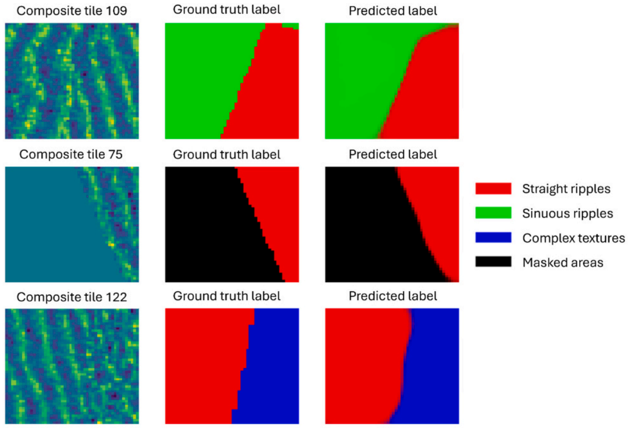

Fig. 6. Sample of 48 × 48 pixels composite tiles (left column) with their respective ground truth label (centre column) and predicted label (right column) from the U-Net model's validation set.

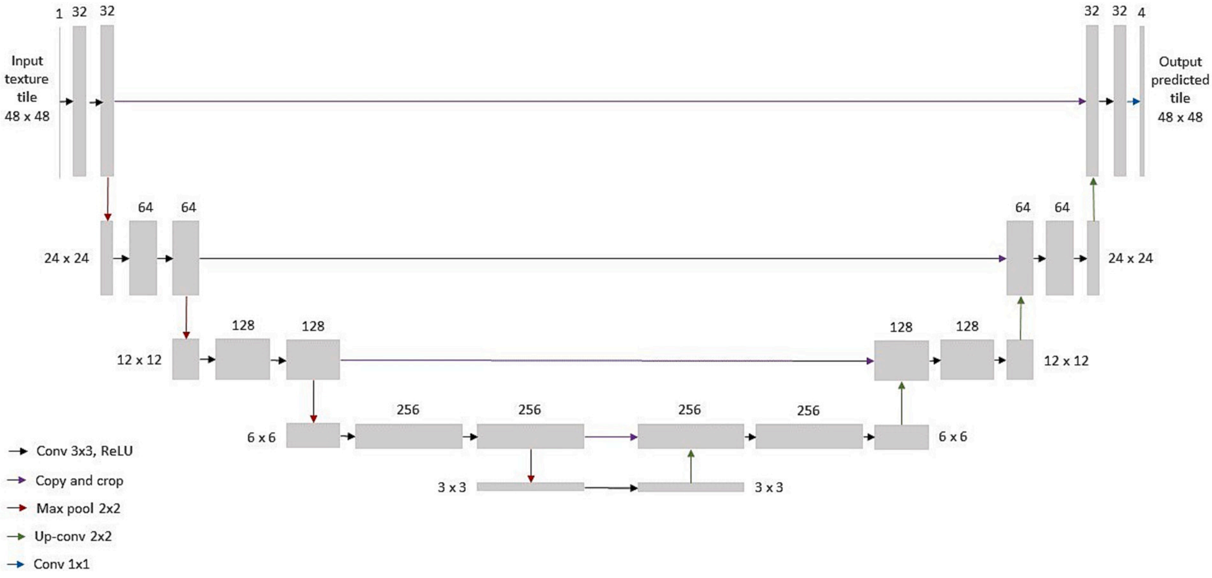

Fig. 5. The U-Net architecture for an input tile of 48 × 48 pixels and a 4-layer output, adapted from Ronneberger et al. (2015).

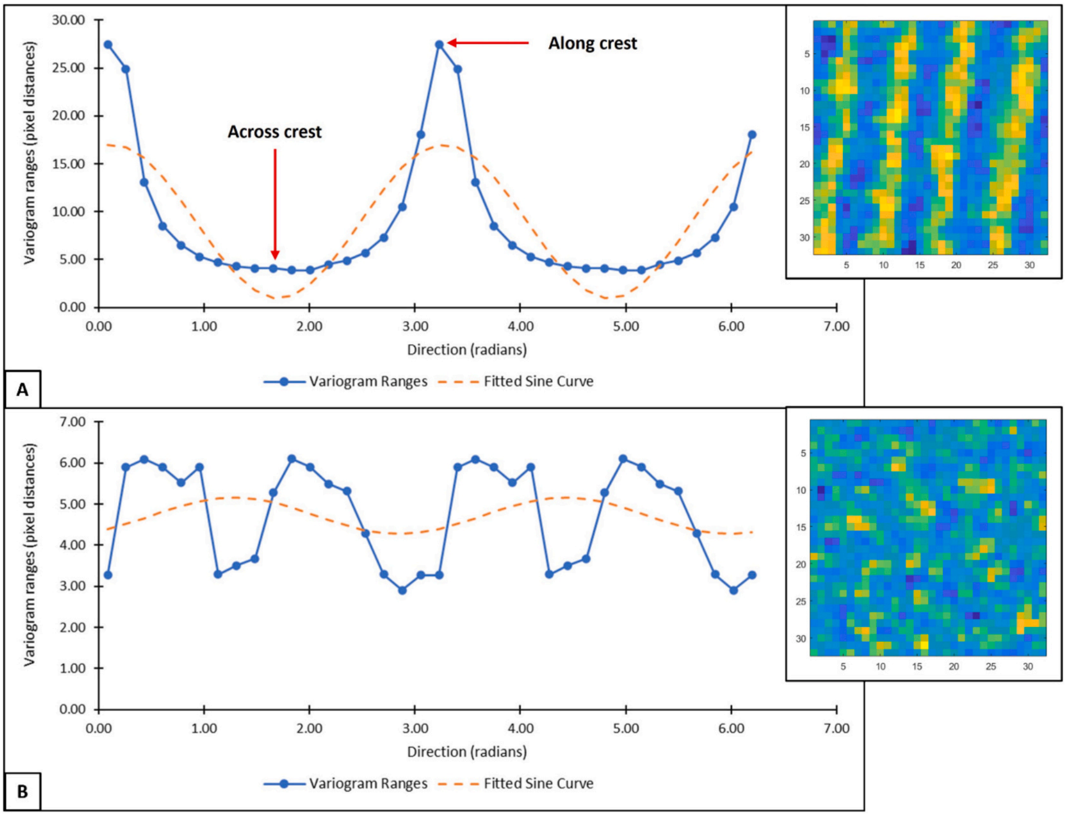

Fig. 7. Examples of the 2D semi-variogram ranges with their sine curves for (A) a straight ripple and (B) complex textures for tile size 32. The insets are the labelled tiles used to generate the respective plots. The ranges are low for straight ripples when oriented across the ripple crest but high when oriented along the crest. For complex textures, the ranges remain relatively the same throughout every orientation. The sine curve fits better to the periodicity of the straight ripple's ranges than to the complex texture's ranges.

Table 1
Confusion matrix and statistical results of the U-Net model's testing set on 400 composites from 15 new tiles for tile sizes 32, 48, and 64.

Label	Tile size	Predicted			Precision	Recall	F1-score
		Straight	Sinuous	Complex			
	32	**0.94**	0.04	0.02	0.63	0.94	0.75
Straight	48	**0.96**	0.01	0.02	0.64	0.96	0.77
	64	**0.95**	0.02	0.03	0.66	0.95	0.78
	32	0.41	**0.56**	0.03	0.77	0.56	0.65
Sinuous	48	0.44	**0.51**	0.06	0.90	0.51	0.65
	64	0.43	**0.46**	0.12	0.89	0.46	0.60
	32	0.14	0.12	**0.74**	0.93	0.74	0.82
Complex	48	0.11	0.04	**0.85**	0.91	0.85	0.88
	64	0.06	0.04	**0.90**	0.86	0.90	0.88

Table 2
Macro averages of the statistical results of the U-Net model's testing set on 400 composites from 15 new tiles for all tile sizes.

Tile size	Macro averages		
	Precision	Recall	F1-score
32	0.78	0.74	0.74
48	**0.82**	**0.77**	**0.77**
64	0.80	0.77	0.75

3.4. U-Net model

3.4.1. Development of the U-Net model

Our first texture segmentation approach was inspired by Karabağ et al. (2019) study, which compared the performance of six traditional segmentation techniques against a supervised U-Net model to segment six texture composites. The results showed that the U-Net model outperformed the traditional techniques, demonstrating superior accuracy in segmenting the textures within the composites.

Model training requires an extensive labelled dataset, typically comprising thousands of samples (Ronneberger et al., 2015), to achieve optimal performance and mitigate overfitting, especially for complex tasks. Therefore, we applied data augmentation to our original dataset, increasing it from 60 to 64,000 tiles, as follows. In addition to the 60 original labelled tiles of three ripple patterns, 20 tiles containing all zeros were created to represent masked areas around the dunes (i.e., where bedrock and rocks were removed), serving as a fourth label type. As we are interested in clearly identifying and differentiating the ripple patterns, we decided to create composite texture tiles as in Karabağ et al. (2019) study. The synthetic training data was produced by generating all permutation pairs (all possible arrangements of two random tiles) from the 80 labelled tiles, resulting in 6400 permutation pairs. Then, ten

Table 3
Macro averages of the statistical results of the semi-variogram's training set for five variogram parameter combinations on the 60 original tiles for all tile sizes.

Tile size	Parameter combination	Macro averages		
		Precision	Recall	F1-score
32	Vertical shift/Amplitude/RMSE/Adjusted R^2	0.87	0.87	0.87
	Vertical shift/Amplitude/RMSE	0.87	0.87	0.87
	Amplitude/RMSE	0.84	0.83	0.83
	Vertical shift/Amplitude	0.85	0.85	0.85
	Vertical shift/RMSE	**0.91**	**0.90**	**0.90**
48	Vertical shift/Amplitude/RMSE/Adjusted R^2	0.83	0.80	0.81
	Vertical shift/Amplitude/RMSE	0.81	0.80	0.79
	Amplitude/RMSE	0.80	0.78	0.77
	Vertical shift/Amplitude	0.87	0.87	0.86
	Vertical shift/RMSE	**0.89**	**0.88**	**0.88**
64	Vertical shift/Amplitude/RMSE/Adjusted R^2	0.82	0.80	0.80
	Vertical shift/Amplitude/RMSE	0.78	0.75	0.74
	Amplitude/RMSE	0.74	0.70	0.69
	Vertical shift/Amplitude	0.78	0.75	0.74
	Vertical shift/RMSE	**0.82**	**0.80**	**0.80**

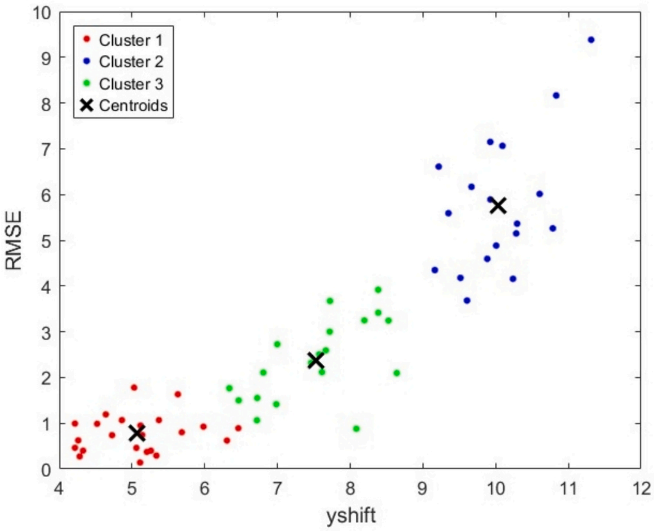

Fig. 8. K-means clustering of the vertical shift and RMSE for the 3 texture categories from the training set for tile size 48. 85 % of all straight ripple labels were grouped into Cluster 2 (in blue), 80 % of sinuous in Cluster 3 (in green), and 100 % of complex textures in Cluster 1 (in red). (For interpretation of the references to colour in this figure legend, the reader is referred to the web version of this article.)

unique random configurations were generated for each pair, where both tiles from the pair are randomly cut and augmented in some way (i.e., flip, crop, scaling, translate, rotate, and shear) to create a new composite tile (Fig. 4). This process yielded 64,000 composite tiles, 90 % of which were set aside for training, and 10 % for validation, for each tile size (32 × 32, 48 × 48, and 64 × 64 pixels).

In the field of machine learning, the training set is used to teach the model, in this case, to recognise the four label types within the composite tiles. The validation set tunes and controls the model, as well as assesses its performance, allowing for adjustments. The algorithm is trained and validated on a large dataset before being applied to independent data for testing which provides an impartial final evaluation of the model. 400 composite tiles were created for the independent test set from fifteen new ripple labelled tiles and five masked area tiles, following the method described in the previous paragraph.

The synthetic data were employed to train a modified U-Net model, which is a convolutional neural network developed by Ronneberger et al. (2015) for biomedical image segmentation. Despite being developed a decade ago, the U-Net model remains in use in aeolian research with good performance rates, as in Daynac et al. (2024), even though more advanced deep learning models are available. Our U-Net model has a similar structure to the original but incorporates a few modifications (Fig. 5). The input dimensions for each layer were adjusted to accommodate 32 × 32, 48 × 48 and 64 × 64 input tiles, with an initial 32 convolutional filters, with a kernel of 3 × 3. Moreover, the overall size of the network was reduced, culminating in a dimension of 3x3x256 at the base of the U-Net. The output predicted tile consists of four layers, one for each texture class (Fig. 5). The model was trained for 50 epochs using categorical cross-entropy as the loss function, and it stabilised quickly; therefore, no more training was required (Fig. S2). Furthermore, by reviewing the U-Net model‘s label predictions on the validation set alongside the manually labelled tile and the original composite tile, the overall label prediction was deemed satisfactory (Fig. 6) and demonstrated that the model has reached a steady state.

3.4.2. Application of the U-Net model

Following training and testing with synthetic data, the model was applied to 42 whole dunes. Each dune is tiled, and every pixel within a sliding window is assigned to one of four classes using one-hot encoding (i.e., if a pixel is assigned to "straight", the "straight" class receives a 1, and the other classes receive a 0). The window size corresponds to the

Table 5
Macro averages of the statistical results of the 2D semi-variogram's testing set of 15 new tiles for all tile sizes.

Tile size	Macro averages		
	Precision	Recall	F1-score
32	0.88	0.87	0.87
48	**1**	**0.87**	**0.92**
64	0.75	0.73	0.72

Table 4
Confusion matrix and statistical results of the 2D semi-variogram's testing set of 15 new tiles for tile sizes 32, 48, and 64.

Label	Tile size	Predicted			Precision	Recall	F1-score
		Straight	Sinuous	Complex			
Straight	32	**1**	0	0	0.83	1	0.91
	48	**0.6**	0.4	0	1	0.6	0.75
	64	**0.4**	0.6	0	0.67	0.4	0.5
Sinuous	32	0.2	**0.8**	0	0.8	0.8	0.8
	48	0	**1**	0	1	1	1
	64	0.2	**0.8**	0	0.57	0.8	0.67
Complex	32	0	0.2	**0.8**	1	0.8	0.89
	48	0	0	**1**	1	1	1
	64	0	0	**1**	1	1	1

Table 6
Confusion matrix and statistical results of the U-Net model's texture classification against visual inspection of 10 test locations for 42 dunes for strides of 12, 8, and 4 pixels.

Observation	Stride size	Predicted				Precision	Recall	F1-score
		Straight	Sinuous	Complex	Unclassified			
Straight	12	**0.87**	0.06	0.03	0.04	0.71	0.87	0.78
	8	**0.87**	0.08	0.03	0.02	0.69	0.87	0.77
	4	**0.86**	0.07	0.03	0.04	0.69	0.86	0.77
Sinuous	12	0.34	**0.58**	0.01	0.08	0.81	0.58	0.67
	8	0.38	**0.53**	0.03	0.06	0.79	0.53	0.63
	4	0.38	**0.54**	0.01	0.07	0.80	0.54	0.65
Complex	12	0	0.06	**0.89**	0.05	0.97	0.89	0.92
	8	0	0.04	**0.91**	0.04	0.95	0.91	0.93
	4	0	0.06	**0.89**	0.05	0.97	0.89	0.93

Table 7
Macro averages of the statistical results of the U-Net model's texture classification against visual inspection of 10 test locations for 42 dunes for all stride sizes.

Stride size	Macro averages		
	Precision	Recall	F1-score
12	**0.83**	**0.78**	**0.79**
8	0.81	0.77	0.78
4	0.82	0.77	0.78

best performing tile size (Section 4.2). The window slides by 4, 8, or 12 pixels, referred to as the stride parameter, and the allocation process is repeated. This method records how many times each pixel is classified into a texture category, and the overlapping tile extraction helps smooth out edge effects in the predictions. With a tile size of 48 pixels, stride sizes of 4, 8, and 12 pixels result in overlaps of 92 %, 83 %, and 75 %, respectively.

3.5. 2D semi-variogram method

A 2D semi-variogram is a spatial autocorrelation analysis that determines characteristic length scales of a mapped variable in different orientations (Matheron, 1963). It has previously been applied to measure the wavelength and height of subaqueous sand waves and ripples (Robert and Richards, 1988; van Dijk et al., 2008). The 2D semi-variogram's 'range' represents the distance at which the semi-variance plateaus, the range will differ depending on the direction being analysed. Due to the nature of the ripple patterns, for straight and sinuous ripples, the range will be quite long when analysing along the ripple crest, but shorter across the crest (Fig. 7A). In other words, the minimum range is a proxy for the minimum pixel distance between the ripple crest and the trough. For complex textures, however, as there is no visual patterning, the ranges will be similar in all orientations (Fig. 7B).

The original 60 labelled ripple tiles for all tile sizes are referred to here as the training set for this method. For each labelled tile, a 2D semi-variogram was executed to measure the ranges for every 10° orientation (from 5° to 355°) of the ripple texture. We used the 'findpeaks' function from the Signal Processing Toolbox in MATLAB (with a minimum peak width of 4 pixels) to record the pixel distance at which the 2D semi-variogram peaks or plateaus (Fig. 7). Differentiating the textures based on the orientation of the absolute minima (across the ripple crest) and maxima (along the ripple crest) from the variogram ranges performed poorly. Therefore, a sine curve was fitted to the ranges (Fig. 7) to calculate several parameters that robustly identify the phase of the minimum and maximum ranges: the vertical shift, the phase shift, the amplitude, the RMSE, and the Adjusted R-squared.

K-means, one of the simplest unsupervised learning models, was applied to the 2D semi-variogram parameters to classify the labelled tiles. It operates as an exclusive clustering algorithm, where each data

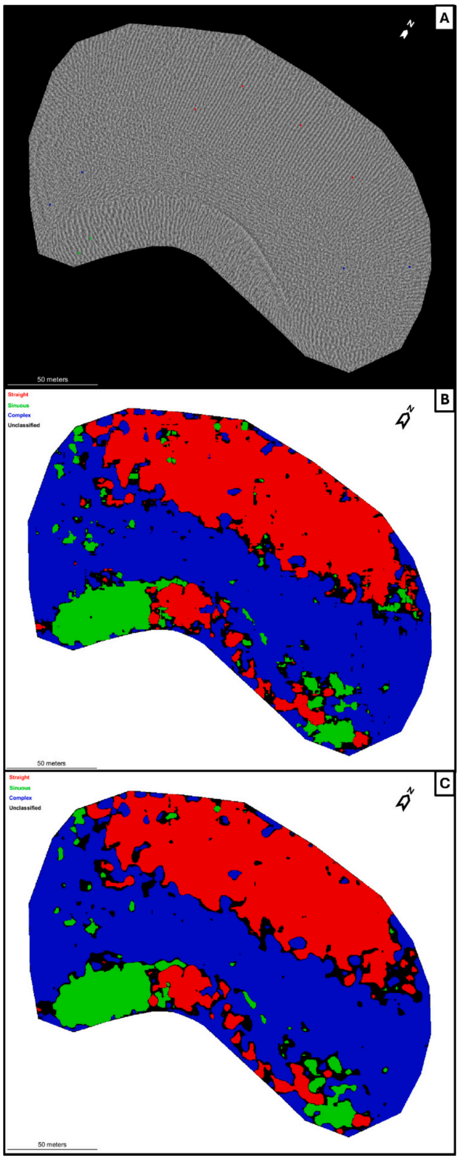

Fig. 9. (A) Grayscale image of the cropped barchan dune from HiRISE image ESP_036411_2560 from the training set with the colour-coded 10 selected ground-truth pixels. (B) Below are the U-Net model's predictions over 50 % of the ripple patterns with a window size of 48 × 48 pixels and a stride parameter of 12 pixels, and (C) a stride parameter of 4 pixels.

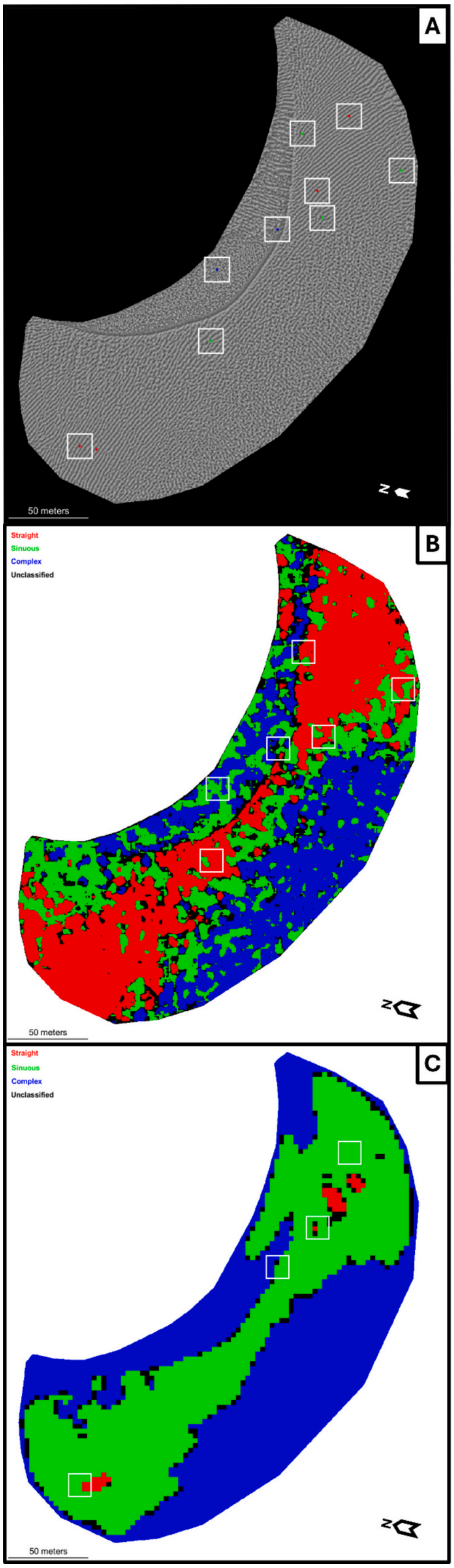

(caption on next column)

Fig. 10. (A) Grayscale image of the cropped barchan dune from HiRISE image PSP_001608_2560 from the training set with the colour-coded 10 selected ground-truth pixels. The pixels that were misclassified by the U-Net model and the 2D semi-variogram are highlighted by white squares. Below are (B) the U-Net model's and (C) 2D semi-variogram's predictions over 50 % of the ripple patterns with a window size of 48 × 48 pixels and a stride parameter of 12 pixels. The 2D semi-variogram's output appears to be overly simplistic compared with the U-Net model's (B). Notably, a significant number of straight ripples are absent from the dune's flanks when compared to the original HiRISE image (A). This discrepancy may be attributed to the 2D semi-variogram's substantial misclassification rates of straight and sinuous ripples (see Table 8 and Section 5.1 of the Discussion for further details).

point is assigned to only one cluster (MacQueen, 1967). The K-means clustering was conducted using different parameter combinations to find the arrangement that successfully groups the labelled tiles into their respective ripple pattern types. The three clusters yielded by the successful parameter combination were then used as a reference to assign new tiles to a ripple class. The 2D semi-variogram was also computed for the 15 labelled tiles from the testing set, and their parameter values were assigned to a ripple class based on the established K-means clusters from the training set.

The 2D semi-variogram was applied to 42 whole dunes following a sliding window approach similar to the U-Net model. The 2D semi-variogram ranges were calculated for the entire sliding window, fitted with a sine curve, and then the vertical shift, phase shift, amplitude, RMSE, and Adjusted R-squared parameters were saved for every pixel within the window. Since there were overlapping pixels, each parameter value was stored multiple times (up to 16 times per pixel for a stride of 12) in a three-dimensional matrix format, resulting in five parameter outputs. Finally, these parameters were classified using K-means and assigned to a class based on the training labelled tiles' clustering reference.

In addition to the ripple classification, the spacing and orientation of the ripples were derived from the 2D semi-variogram's output parameters. The 2D semi-variogram extracts a characteristic length-scale from the textures, but not a wavelength. For straight and sinuous ripples, this value can be interpreted as a spacing. However, for complex textures, while this value is not considered a 'spacing,' it still represents a characteristic length scale. Ripple spacings are measured from one ripple crest to the next; however, the 2D semi-variogram measures the distance between a ripple crest and its trough, i.e., the minimum range (Fig. 7). Therefore, we calculated the spacing by taking the average of the three y values of the sine curve located around the minimum range, times two. These spacings were converted from pixels to meters and plotted against manual measurements of the straight and sinuous ripple tiles to determine the closest correlation. The manual measurements involved taking the average of three transects, with each transect being separated by three ripple crests. The orientation of the ripples, specifically the crest alignment orientation of the ripples, transverse to the assumed direction of ripple migration, was measured by the output phase shift from −90° to +90°. These results were evaluated against manual measurements of the labelled tiles.

3.6. Statistical analysis of the texture segmentation methods

3.6.1. Selection of the best labelled tile size

The accuracy of the labelled tile classification was assessed for both methods on the testing set, which included 400 composites for the U-Net model and 15 tiles for the 2D semi-variogram. Results on the validation data are located in the supplementary material (Tables S2–S5). These evaluations were done across the three different tile sizes (32 × 32, 48 × 48, and 64 × 64 pixels) using confusion matrices. For the U-Net model, the confusion matrices recorded the number of times a pixel within a composite tile was classified as True Positive (TP), False Positive (FP), True Negative (TN), and False Negative (FN). For the 2D semi-

Table 8
Confusion matrix and statistical results of the 2D semi-variogram's texture classification against visual inspection of 10 test locations for 42 dunes for strides of 12 and 8 pixels, and for 10 dunes for stride of 4 pixels.

Observation	Stride size	Predicted				Precision	Recall	F1-score
		Straight	Sinuous	Complex	Unclassified			
	12	**0.02**	0.82	0.13	0.03	1	0.02	0.05
Straight	8	**0.02**	0.83	0.13	0.02	1	0.02	0.05
	4	**0.03**	0.84	0.13	0	1	0.03	0.06
	12	0	**0.40**	0.54	0.06	0.33	0.40	0.36
Sinuous	8	0	**0.44**	0.53	0.03	0.34	0.44	0.38
	4	0	**0.43**	0.57	0	0.33	0.43	0.38
	12	0	0.01	**0.97**	0.02	0.29	0.97	0.45
Complex	8	0	0.01	**0.99**	0	0.29	0.99	0.44
	4	0	0	**1**	0	0.28	1	0.44

Table 9
Macro averages of the statistical results of the 2D semi-variogram's texture classification against visual inspection of 10 test locations for 42 dunes for all stride sizes.

Stride size	Macro averages		
	Precision	Recall	F1-score
12	0.54	0.46	0.28
8	0.54	0.48	0.29
4	**0.54**	**0.49**	**0.29**

variogram, however, the confusion matrices recorded the number of times a whole labelled tile was correctly classified. The precision, recall, and F1-score were calculated for each pattern type from these confusion matrices to evaluate the influence of tile size on label predictions (Cao et al., 2024; Nagle-Mcnaughton et al., 2020; Tang et al., 2023). Precision measures the model's reliability by determining the ratio of correctly predicted true positives over all positive predictions (Eq. (1)). Recall calculates the model's detection rate by taking the ratio of correctly predicted true positives over the total number of positive samples (Eq. (2)). The F1-score assesses the model's overall performance and the trade-offs between precision and recall by computing the harmonic mean of the two (Eq. (3)). Finally, the best tile size was chosen based on its macro average of the precision, recall and F1-score metrics by taking the arithmetic mean of all classes (i.e., straight ripples, sinuous ripples, and complex textures).

$$Precision = \frac{TP}{(TP + FP)} \tag{1}$$

$$Recall = \frac{TP}{(TP + FN)} \tag{2}$$

$$F1\ score = 2 \times \frac{(Precision \times Recall)}{(Precision + Recall)} \tag{3}$$

3.6.2. Evaluation of the dune mapping

To assess the impact of overlapping ripple predictions (i.e., the stride parameter) on dune classification, the performance of both texture segmentation methods was compared against manual observations from 42 dunes. This included all nine dunes from the testing dataset, along with 33 dunes from the training dataset. During the survey of each dune, areas exhibiting distinct ripple patterns were identified, and the pixel located at the centre of each identified area was manually classified. Test locations were carefully selected to ensure coverage across various dune features, including the horns, flanks, and stoss slope. Given that the number of distinct ripple patterns varies among the dunes, we capped the manually selected test locations at 10 per dune, resulting in 420-test classifications. In total, there were 130 test locations for straight ripples, 131 for sinuous ripples, and 159 for complex textures. 19 dunes from the training dataset were previously used to create training tiles for the U-Net model and 2D semi-variogram; therefore, we ensured that the new 420-test locations did not overlap with the locations of the training tiles.

Both the U-Net's and 2D semi-variogram's outputs recorded the number of times a pixel has been classified in the third dimension. A threshold was set to 50 % on these outputs, thus if a pixel was assigned over 50 % of the time to one texture category, the output would record that category. If a pixel has not reached that threshold, meaning that the allocation has not been consistent between overlaps, the output was categorised as 'unclassified'. For strides of 4, 8, and 12 pixels, the 50 % threshold outputs from both the U-Net and 2D semi-variogram were checked against the 420-test locations. To determine the accuracy of the pixel assignments, the precision, recall, F1-score, and macro-average were computed from the confusion matrices.

4. Results

4.1. Classifying tile patterns

4.1.1. U-Net model's best tile size selection

The U-Net model frequently misclassified sinuous ripples as straight in the testing set, occurring up to 43 % of the time for tile size 48 (Table 1). This misclassification has significantly decreased the Precision values for straight ripples and the Recall values for sinuous ripples, for all tile sizes (Table 1). Nonetheless, the macro averages range between 74 % and 82 % for all tile sizes, with the 48-tile size achieving slightly better performance with 82 %, 77 %, and 77 % for precision, recall, and F1-score, respectively (Table 2).

4.1.2. K-means clustering on the 2D semi-variogram parameters

For the 2D semi-variogram, K-means clustering achieved the best outcome on the training tiles with the vertical shift and RMSE parameters combination for all tile sizes when analysing the macro-averages of the precision, recall and F1-score (Table 3). Consequently, the 3 clusters from that K-means combination were used as the benchmark for assigning the testing tiles to a ripple class (Fig. 8 for the 48-tile size).

4.1.3. 2D semi-variogram best tile size selection

Straight ripples from the testing set were erroneously identified as sinuous 40 % and 60 % of the time for tile sizes 48 and 64, respectively, with the 2D semi-variogram (Table 4). These misclassifications affected the straight ripple recall results for both tiles 48 and 64. Despite these misclassifications, the macro averages range between 72 % and 100 % for all tile sizes, with the 48-tile size achieving slightly better performance with 100 %, 87 %, and 92 % for precision, recall, and F1-score, respectively (Table 5).

As both the U-Net model and the 2D semi-variogram performed better on the testing set with the 48-tile size, the sliding window was set to 48 × 48 pixels when applying the classification to whole dunes.

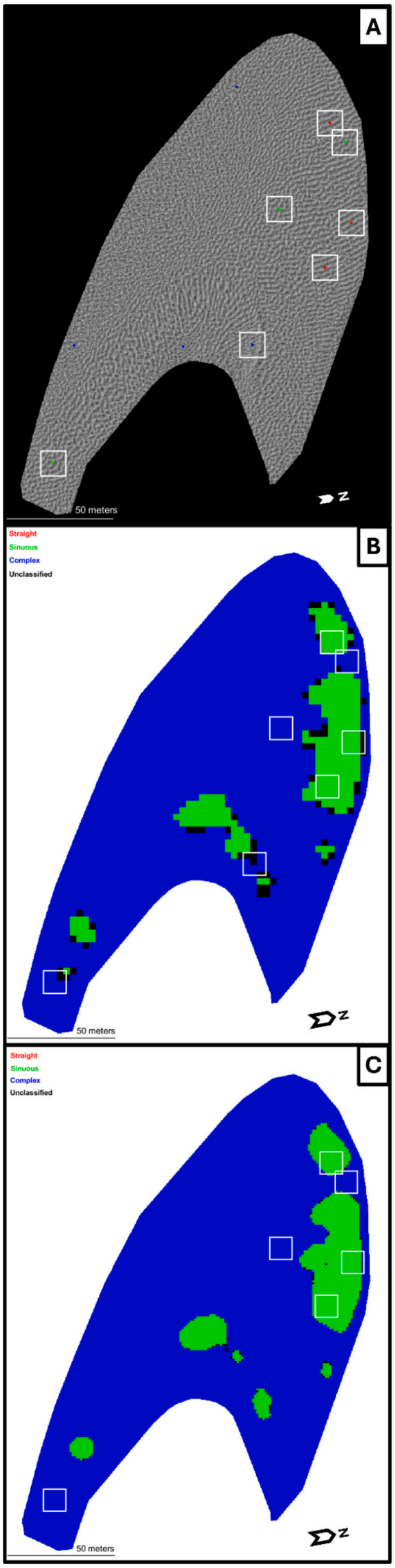

Fig. 11. (A) Grayscale image of the cropped barchan dune from HiRISE image ESP_036109_2550 from the training set with the colour-coded 10 selected ground-truth pixels. The pixels that were misclassified by the 2D semi-variogram are highlighted by white squares. (B) Below are the semi-variogram's predictions over 50 % of the ripple patterns with a window size of 48 × 48 pixels and a stride parameter of 12 pixels, and (C) a stride parameter of 4 pixels.

4.2. Classifying patterns within a whole dune

4.2.1. Evaluation of the U-Net model's dune mapping results

The prediction model was applied directly to 42 whole dunes for tiles of 48 × 48 pixels and a stride of 4, 8 and then 12 pixels. A confusion matrix was created for the 420-test comparisons for each stride size, and the precision, recall, and F1-score were computed to evaluate the impact of the stride on dune classification. Similar to the tile classification results (Section 4.1.1), the U-Net model misclassified between 34 % and 38 % of sinuous pixels as straight for all stride sizes, affecting recall and F1-score values (Table 6). In addition, instances were found where all three texture categories were unclassified for all stride sizes (Table 6), indicating inconsistencies in the U-Net model's allocation of pixels to specific categories. However, the macro-averages for all stride sizes showed similar high precision (81–83 %), recall (77–78 %), and F1-score (78–79 %), with slightly higher scores observed for the 12-pixel stride (Table 7). This minimal difference between the macro-averages for all stride sizes is reflected in the dune ripple maps (Fig. 10).

Fig. 9 shows an example where the U-Net model accurately classifies all 10 selected pixels (Fig. 9A) for all three stride sizes. The model effectively located the ripple patterns on the dune, with minimal differences in the output between stride sizes (12 pixel and 4 pixel strides in Fig. 9B and C, respectively), beyond a slight increase in unclassified areas and smoother boundaries as the stride size decreased. These unclassified pixels are mainly located on the boundary between two textures, and thus may reflect the transition from one ripple type to the next. The complex textures are primarily concentrated in a band across the centre of the dune, with straight ripples at the top of the image with some patches from the middle of the slip face to the right horn, and sinuous ripples mainly on the left of the slipface with patches on the right horn and left flank of the dune.

However, on the other hand, the U-Net model performed the worst with dune 1 from the HiRISE image PSP_001608_2560 (Fig. 10A), misclassifying 6 out of 10 test locations for all three stride sizes (12 pixel stride in Fig. 10B). Despite this, the main areas of straight ripples and complex textures are still represented, but the classification is noisier compared to the previous dune (Fig. 9). Like in the previous case, there are minimal differences between the stride outputs, with a slight increase in unclassified areas and smoother boundaries as the stride parameter size decreased (Fig. S3). Due to the minimal differences between the stride sizes for pixel allocation and visual outputs, a larger stride size, such as 12 pixels, is sufficient to accurately classify textures over the dunes. This also helps conserve computational time and energy during model execution.

4.2.2. Evaluation of the 2D semi-variogram's dune mapping results

In line with the U-Net model, the 2D semi-variogram was applied directly to 42 complete dunes for a tile of 48 × 48 pixels with a stride of 12 and 8 pixels. Due to computational cost and time constraints, a stride of 4 pixels was used for only 10 dunes. However, with the same allocation threshold of 50 %, the 2D semi-variogram method poorly classified the 420-pixel observations for all three stride sizes (Table 8). The macro-averages were consistent across all stride sizes, with precision at 54 %, recall ranging from 46 % to 49 %, and F1-score from 28 % to 29 % (Table 9). Slightly higher statistical scores were achieved with a 4-pixel stride (Table 9). These underwhelming results can be attributed to the straight ripples being correctly classified only 2–3 % of the time (Table 8) and being misclassified 82–84 % as sinuous (up from 40 % when selecting the best tile size in Section 4.1.3), an example of this represented in Fig. 10. Sinuous ripples were also frequently misclassified as complex textures, 54 % to 57 % of the time, whereas complex textures achieved near-perfect results with ≥97 % correct classifications (Table 8). There were slightly fewer instances where all three texture categories were unclassified for all stride sizes compared with the U-Net model (0–6 % in Table 8 vs 2–8 % in Table 6), indicating irregularity in the 2D semi-variogram's ability to allocate the selected pixels to a single

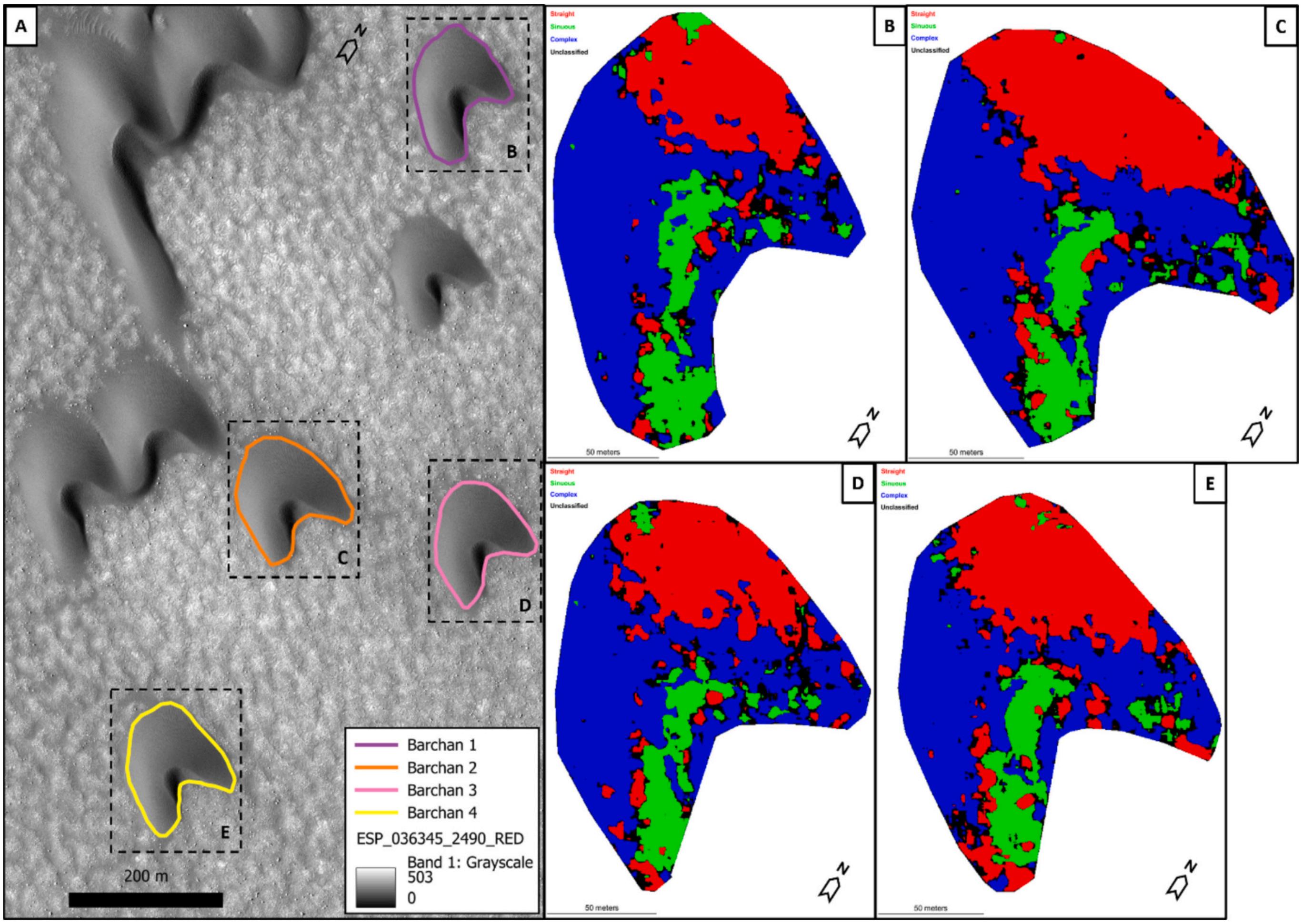

Fig. 12. (A) HiRISE image ESP_036345_2490 with four barchan dunes outlined that have been used to map ripple patterns. U-Net model's classification of texture with a 48 × 48 pixel tile size and a stride of 12 pixels for (B) Dune 1, (C) Dune 2, (D) Dune 3, and (E) Dune 4. Note: these dunes have ripples on the slipface, which may denote a complex wind regime, despite the assumed unidirectional wind flow characteristic of barchan dunes.

category.

Looking at specific dune examples, dune 1 of the HiRISE image PSP_001608_2560 (Fig. 10A) was one of the best segmented dunes by the 2D semi-variogram, with 6 out of the 10 selected pixels accurately classified for strides of 12 (Fig. 10C), and 7 out of 10 with a stride of 8. Due to the large size of the dune, a stride of 4 pixels was not applied as it was too computationally expensive. The output from stride 12 appears coarser and contains slightly more unclassified areas than the output from stride 8 (Fig. S4). The texture regions are roughly defined, but the majority of the straight ripples are missing from the dune's flanks compared to the original HiRISE image (Fig. 10A) and the U-Net's outputs (Fig. 10B).

Conversely, the 2D semi-variogram performed the worst on dune 3 from the HiRISE image ESP_036109_2550 (Fig. 11A), misclassifying 7 out of 10 test locations with a stride of 12 (Fig. 11B), and 6 out of 10 pixels with a stride of 4 (Fig. 11C). Similar to the previous dune, unclassified areas decrease, and the texture region boundaries become smoother as the stride size decreases (Fig. 11). Straight ripples are absent in the classification, even though some are visible on the right flank of the dune in the HiRISE imagery. Furthermore, some sinuous ripples are also missing on the left horn, stoss slope and right flank. Despite improvements in performance with smaller stride sizes, the 2D semi-variogram's limitations include increased computational cost, overall misclassification of texture, and poor statistical results, rendering it unsuitable for mapping ripple patterns.

4.2.3. *Consistency in the classification of neighbouring dunes*

For barchan dunes located within the same region of a dunefield, as illustrated in HiRISE image ESP_036345_2490 (Fig. 12A), the U-Net model's classification of these dunes' texture yields very similar results (Fig. 12B-E). Across all four dunes, straight ripples are predominantly located at the top right, sinuous ripples appear near the slipface and on the left horn among some patches of straight ripples, and complex textures are observed on the left flank, slipface, and some patches on the right horn. The topography of upwind dunes (Fig. 12A) would impact the wind flow to varying degrees and consequently influence the formation of ripples. It is assumed that dunes in close proximity are shaped by the same wind regime and thus would display similar ripple patterns. As the U-Net's classification outputs showcase this consistency in the distribution of the ripple patterns across multiple dunes, it corroborates the model's ability to identify texture in this context.

4.3. *Spacing and orientation from the 2D semi-variogram*

4.3.1. *Evaluation against manual measurements of the labelled tiles*

Due to their nature, we cannot interpret the spacing and orientation of the complex textures. Therefore, we focused solely on the straight and sinuous labelled tiles in the training set (40 tiles) and testing set (10 tiles). The ripple crest orientations computed from the phase shift of the 2D semi-variogram's sine curve matched the manual measurements (Fig. 13A), with a correlation coefficient of 0.98 for tile size 48 (Fig. 13B). Our method to measure the spacing was strongly correlated

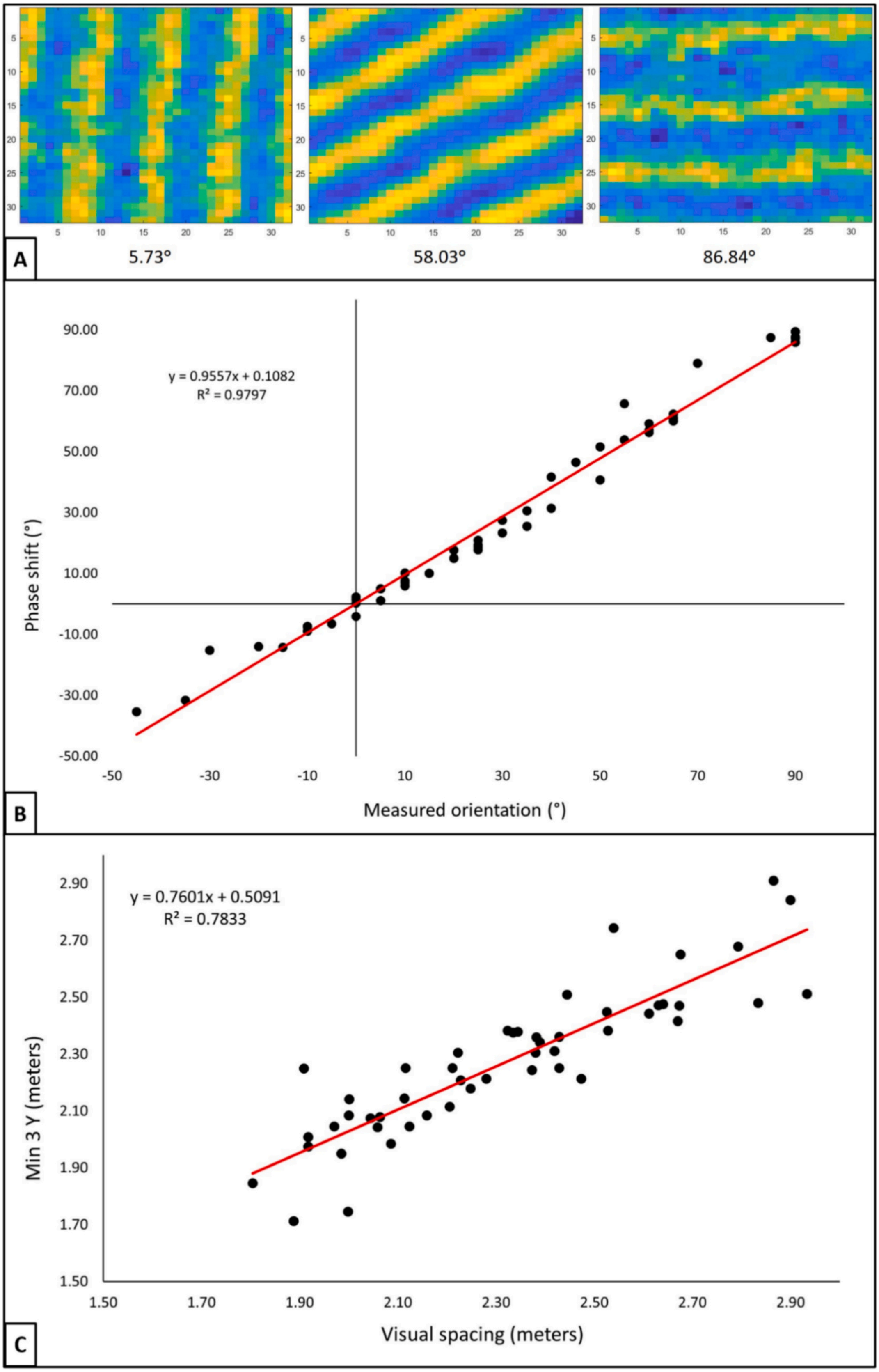

Fig. 13. (A) Samples of ripple labelled tiles with their corresponding crest alignment orientation value. 0° is at the top of the image (north), and +/− 90° corresponds to the sides of the image (east-west). (B) Phase shift from the semi-variogram's sine curve against measured orientation for tile size 48. (C) Average of the minimum three Y values against visual spacing for tile size 48.

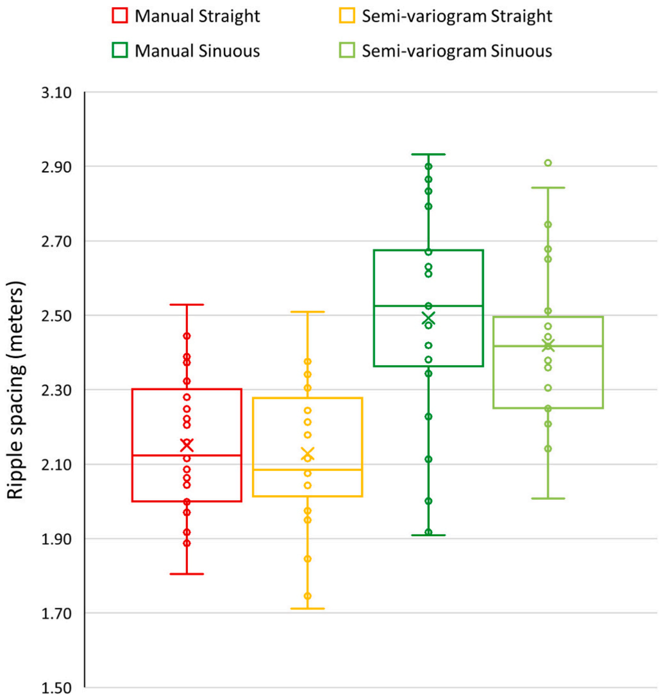

Fig. 14. Box plots of the manual spacing measurements and semi-variogram spacing of straight ripples (in red and orange, respectively) and sinuous ripples (in dark green and light green, respectively) in pixels for tile size 48. (For interpretation of the references to colour in this figure legend, the reader is referred to the web version of this article.)

with the manual spacing measurements across all three tile sizes, with a correlation coefficient of 0.78 for tile size 48 (Fig. 13C). Therefore, when applying the 2D semi-variogram to whole dunes, we were confident that the derived spacing and orientation were accurate.

4.3.2. *Application of the spacing and orientation to whole dunes*

Upon reviewing the manual spacing measurements of the ripple labelled tiles, we observed that straight ripples generally have smaller spacings than sinuous ripples (Fig. 14). At present, the physical mechanisms and variables that control the sinuosity and spacing of meter-scale ripples at the local level on Mars remain poorly understood, and these factors may differ from those observed on Earth. However, our visual analysis of classification outputs revealed that sinuous ripples were often situated on the slipface (examples in Fig. 15), indicating that the slope angle and gravity likely influenced the curvature and spacing of the ripples.

As the U-Net model produced better results for classifying ripples, the spacing and orientation of ripples are only represented for the straight and sinuous ripples identified with the U-Net model. For the four dunes in HiRISE image ESP_036345_2490, which all had a consistent ripple pattern distribution (Fig. 12), their spacing and direction values are also similarly distributed over the dunes (Fig. 15). The greatest spacings (>2.5 m) are observed on the slipface and the left horn of the dunes (Fig. 15) where sinuous ripples are concentrated (Fig. 12). The orientation denoted here represents the alignment of the ripples; specifically, it is parallel to the crestline of the ripples. Due to their slow migration, ripples on Mars can integrate different wind directions and have been observed to migrate longitudinally, in contradiction to the transverse motion of terrestrial ripples (Silvestro et al., 2016). Therefore, we refrain from interpreting the migration direction of the mapped ripples and instead focus on their crestline orientation. Interestingly, the orientation of the sinuous ripples on the slipface shifts from −20° (in blue) on the northern side to 30°-40° (in red) on the southern side (Fig. 15). The left horn has less contrasting ripple orientations, ranging from −10° to 10°, and the right flank of the dunes, where the straight ripples are located (Fig. 12), orientations range from 0° to 40° (Fig. 15). This consistency in the spacing and orientation values for neighbouring dunes confirms the ability of the 2D semi-variogram to extract characteristics from the ripple patterns.

5. Discussion

Sand ripples are universal bedforms on the surfaces of dunes on Earth and Mars. They display a range of textures and patterns, indicative of the flow regime that shaped them. In this study, we segmented and characterised three ripple patterns over barchan dunes on Mars.

5.1. *The classification performance between both methods*

In the first stage of classifying labelled tiles to select the best tile size, although sinuous ripples in the testing set were misclassified as straight for the U-Net model (Table 1) and vice versa for the 2D semi-variogram (Table 4), both methods produced results ≥72 % for all tile sizes (Tables 2 and 5). The performance difference between the methods became evident in the second stage of mapping patterns over a whole dune. The U-Net model achieved macro-average results of 81–83 %, 77–78 %, and 78–79 % for precision, recall, and F1-score, respectively (Table 7). These results are comparable to findings from other studies using CNN models to classify dune types on Earth (Tang et al., 2023) and terrestrial dune patterns (Zheng et al., 2024b), outline terrestrial dunes (Daynac et al., 2024) and isolated barchan dunes on Mars (Rubanenko et al., 2021) or extract Transverse Aeolian Ridges (Cao et al., 2024).

In Karabağ et al. (2019)'s study, some configurations of the U-Net model produced texture segmentation results that outperformed traditional algorithms, although this was not the case for all configurations. As our model was inspired by Karabağ et al. (2019), we anticipated some differences in mapping results between the U-Net model and the 2D semi-variogram, but the extent of the discrepancy was unexpected. The macro-average results for the 2D semi-variogram only reached 54 %, 46–49 %, and 28–29 % for precision, recall, and F1-score, respectively (Table 9). These outcomes are significantly lower than those reported in studies using other signal processing methods to segment bedforms, such as Radon transform to map dune field patterns (Gadhiraju et al., 2014).

The misclassification of both straight and sinuous ripples in the dune mappings for each method may be attributed to the subjective nature of the labelled training tiles, which might overlook characteristics that are not visually discernible. In addition, a clear separation between straight and sinuous ripples is difficult, as there is a transition between these patterns. This transition between the patterns may also be reflected by the unclassified pixels that are mainly found at the boundaries between two textures in the U-Net model's dune mappings (Figs. 9B-C and 10B).

The degree of segmentation between the U-Net model and 2D semi-variogram varies significantly. The dune mappings generated by the 2D semi-variogram appear overly simplistic when compared to those produced by the U-Net model (Fig. 10). Furthermore, a substantial portion of the classifications by the 2D semi-variogram was inaccurate, with up to 98 % of straight ripples and 57 % of sinuous ripples misclassified (Table 8). In addition, slight variations were noticed in the ripple classification across different iterations of the 2D semi-variogram analysis for the same dune. Consequently, this method is considered unsuitable for accurately mapping ripples. In the authors' opinion, the U-Net model offers a reasonable classification of the actual distribution of ripple patterns across most dunes, albeit with slightly more noise, particularly at the transitional boundaries between different textures (Figs. 9 and 10A-B). The high degree of fragmentation observed in the segmentations produced by the U-Net model could potentially be mitigated by smoothing the outputs to eliminate outliers (for instance, 1–4 straight pixels within a cluster of sinuous pixels). However, implementing this process would necessitate additional assumptions and parameter testing

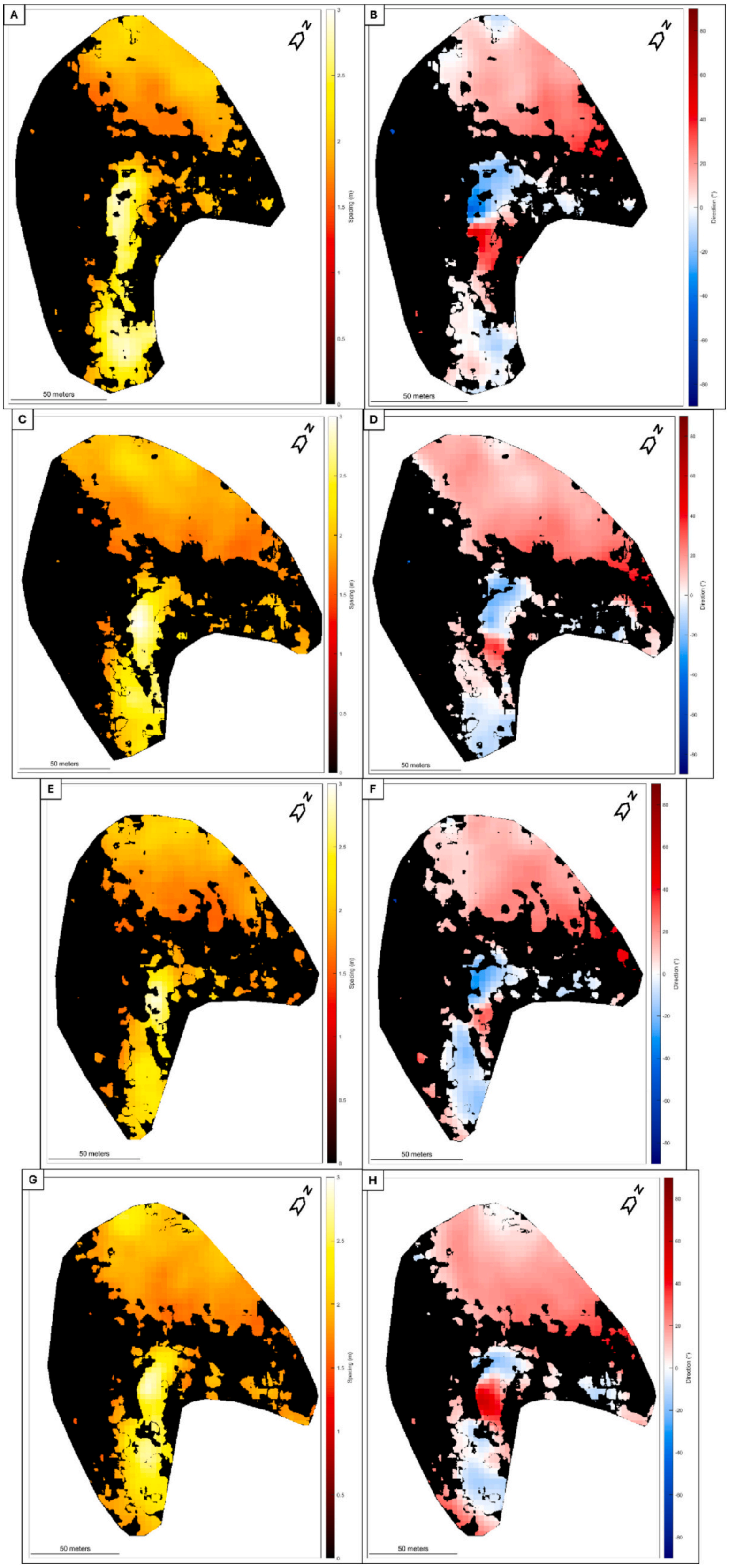

Fig. 15. (A, C, E, G) The ripple spacing in meters and (B, D, F, H) ripple orientation in degrees are computed from the 2D semi-variogram for (A-B) Dune 1, (C-D) Dune 2, (E-F) Dune 3, and (G-H) Dune 4 from HiRISE image ESP_036345_2490. Only the straight and sinuous ripples segmented by the U-Net model that reached the 50 % threshold are displayed. Complex textures and unclassified areas are represented in black.

related to ripple mapping.

The U-Net model's ability to accurately map ripple patterns on multiple neighbouring dunes (Fig. 12), likely shaped by the same wind regime, offers the potential to analyse and compare ripple distribution across extensive regions of Mars. In addition, after being trained on labelled tiles, the U-net model only requires a few seconds to map ripples per dune, in contrast to the 2D semi-variogram, which took up to 3 h for a 12-pixel stride. Although the 2D semi-variogram did not effectively classify ripple patterns, its precise measurement of spacing ($R^2 = 0.78$) and orientation ($R^2 = 0.98$) of straight and sinuous ripples (Fig. 13) allows meaningful investigation into sand transport conditions on Martian dunes.

5.2. Linking the pattern parameters extracted by 2D semi-variogram with previous studies on Martian sand ripples

The ripple spacings determined from the 2D semi-variogram dune mappings (Fig. 15) range from 1.7 m to 3 m, consistent with ripple wavelengths measured in many other studies on Martian barchans. Ripples on barchan and barchanoid dunes in Herschel crater also have wavelengths ranging from 1.7 to 3 m (Silvestro et al., 2011; Vaz et al., 2017), as well as in Lyot Crater (Vaz et al., 2023). At Gale Crater, ripple wavelengths were measured to range from 1.9 m (Silvestro et al., 2016) to 2.6 m (Sullivan et al., 2020), and were 2 m in Hellespontus Montes (Rubanenko et al., 2022). Furthermore, the two contrasting ripple orientations mapped on barchan dunes (~60° difference, Fig. 15), have also been measured in Herschel Crater with bidirectional ripples at 90° (Cardinale et al., 2020). At Meridiani Planum, the ripples displayed a clear square pattern with a 105° direction difference (Silvestro et al., 2011), a pattern also observed in Gale Crater which may be due to the reworking of the ripples by a secondary wind direction (Silvestro et al., 2016).

Five of these studies have automatically measured the wavelength and/or orientations of ripples. The ripple crestlines were either segmented and characterised through wavelet transform edge analysis and morphological multiscale gradient (Silvestro et al., 2011) or via an Object Based Image Analysis (OBIA) approach (Silvestro et al., 2016; Vaz et al., 2017; Cardinale et al., 2020). However, a drawback of these methods is the delineation of each individual ripple crestline, which then requires generalisation over a larger area, and can result in an overwhelming amount of data when analysing extensive images. In contrast, the 2D Fast Fourier Transform method (Vaz et al., 2023) bears the closest resemblance to our 2D semi-variogram, as it measures the wavelength of a group of ripples rather than each individual ripple, thereby facilitating more manageable subsequent analysis. At present, our 2D semi-variogram method is computationally intensive; thus, future work will explore the use of the 2D Fast Fourier Transform for measuring the spacing and orientation of ripples.

5.3. Limitations of this study

This study's methodology was only trained and tested to recognise three pattern types on 42 barchan dunes from 6 locations within the North Polar Region of Mars. Our approach was specifically designed for images of sand surfaces and may not be as effective for surfaces containing rocks, vegetation, or other features that could be mistakenly identified as part of a pattern. The classification of straight, sinuous, and complex textures was inspired by previous ripple research conducted on Mars (Silvestro et al., 2016; Vaz et al., 2017; Hood et al., 2021). However, we are uncertain about the efficacy of our method when applied to patterns not included in our current classification. For example, a square ripple pattern has been identified on barchanoids within craters (Silvestro et al., 2016), but to the authors' knowledge, not within the northern polar region. Consequently, if this pattern is found to be predominant among dunes in craters, it would require the creation of a fourth category for square patterns to optimise the classification results.

The training dataset, consisting of 60 labelled tiles, was relatively small and relied on our visual assessment of textures and pattern types. To enhance the U-Net model's performance, permutation pairs were created and augmented, thereby expanding the training dataset and the model's pattern recognition capabilities. This difference in training data size may account for the 2D semi-variogram's limited success in classifying ripples over whole dunes.

5.4. Potential application of the methods

We aim to expand our methods to include more Martian sites and imagery from terrestrial unmanned aerial vehicles, enabling the comparison of ripple patterns across planets and making inferences about sand transport conditions. Our current study uses HiRISE images with a resolution of 0.25 m per pixel, sufficient to identify ripples spaced 1.6 to 3 m apart. While some HiRISE images have a resolution of 0.5 m per pixel, which may impede ripple detection, future research will focus on high-resolution Martian sites. Our methodology can also be adapted for drone imagery (after filtering and standardization) or coarser satellite imagery to map larger features, such as dune fields or vegetation patterns on Earth. Mapping patterns in spatial ecology has become an important field of study (Tarnita, 2024) to understand tipping points in complex systems. For example, ecosystems that have a regular spatial structure alternating high and low biomass are more productive and resilient to global change (Rietkerk et al., 2021).

Our findings show that the U-net model effectively analyses and segments patterns within large datasets. Furthermore, by augmenting a small, labelled training dataset, we can achieve high classification accuracy. Conversely, the 2D semi-variogram is better for extracting quantifiable variables like pattern spacing or orientation from smaller datasets, due to its higher computational cost. Both methods can work together in studies that categorise textures across large surfaces and extract variables from specific textures.

6. Conclusions

Ripple patterns provide valuable insight into local sand transport conditions, offering a unique opportunity to enhance our understanding of wind regimes on Mars and Earth, especially in areas where direct wind observations are not feasible. However, manually mapping these ripples is not only time-consuming but also subjective. Our objective was to quantify three types of ripple patterns - straight ripples, sinuous ripples, and complex textures - and map their distribution over barchan dunes. We present two innovative and complementary methods for identifying these ripple patterns on high-resolution satellite imagery (HiRISE) of Martian dunes. The performance of both methods was evaluated using 42 barchan dunes from six HiRISE sites on Mars.

The first approach, a machine learning model known as U-Net, demonstrated greater reliability in classifying the ripple patterns over whole dunes, achieving 83 % for precision, 73 % recall, and 79 % F1-score. The second approach, a spatial autocorrelation analysis called 2D semi-variogram, poorly classified the ripple patterns over whole dunes (up to 54 % for precision, 49 % recall, and 29 % F1-score), but allowed for correctly measuring the ripple spacing ($R^2 = 0.78$) and orientation ($R^2 = 0.98$).

By leveraging the efficiency of the U-Net model in ripple classification and the 2D semi-variogram's precision in measuring spacing and orientation, extensive analysis of ripples and local wind regimes can be conducted across Mars. Moreover, these methods can also be applied to drone imagery of terrestrial dunes or to other patterned features, offering a promising avenue for further research and exploration.

CRediT authorship contribution statement

Lucie A. Delobel: Writing – review & editing, Writing – original draft, Visualization, Validation, Software, Resources, Methodology, Investigation, Formal analysis, Data curation, Conceptualization. **David Moffat:** Writing – review & editing, Visualization, Validation, Software, Resources, Methodology, Formal analysis, Data curation. **Emma Tebbs:** Writing – review & editing, Supervision. **Andreas C.W. Baas:** Writing – review & editing, Validation, Supervision, Software, Methodology, Investigation, Formal analysis, Conceptualization.

Funding

This research did not receive any specific grant from funding agencies in the public, commercial, or not-for-profit sectors.

Declaration of competing interest

The authors declare that they have no known competing financial interests or personal relationships that could have appeared to influence the work reported in this paper.

Acknowledgements

This work was supported by the NERC Earth Observation Data Acquisition and Analysis Service (NEODAAS) for the development and implementation of the U-Net model. The authors thank the five reviewers for their contributions to improving this work.

Appendix A. Supplementary data

Supplementary data to this article can be found online at https://doi.org/10.1016/j.rse.2025.115031.

Data availability

Data will be made available on request.

References

Allen, J.R.L., 1963. Asymmetrical ripple marks and the origin of water-laid cosets of cross-strata. Geol. J. 3, 187–236.

Allen, J.R.L., 1968. Current Ripples: Their Relation to Patterns of Water and Sediment Motion. North-Holland Publishing Company.

Cao, Z., Kang, Z., Hu, T., Yang, Z., Chen, D., Ren, X., Meng, Q., Wang, D., 2024. AiTARs-Net: a novel network for detecting arbitrary-oriented transverse aeolian ridges from Tianwen-1 HiRIC images. ISPRS J. Photogramm. Remote Sens. 211, 135–155. https://doi.org/10.1016/j.isprsjprs.2024.03.021.

Cardinale, M., Pozzobon, R., Tangari, A.C., Runyon, K., Di Primio, M., Marinangeli, L., 2020. Reconstruction of the sand transport pathways and provenance in Moreux crater, Mars. Planet. Space Sci. 181, 1–15. https://doi.org/10.1016/j.pss.2019.104788.

Cataño-Lopera, Y.A., Abad, J.D., García, M.H., 2009. Characterization of bedform morphology generated under combined flows and currents using wavelet analysis. Ocean Eng. 36, 617–632. https://doi.org/10.1016/j.oceaneng.2009.01.014.

Cazenave, P.W., Dix, J.K., Lambkin, D.O., Mcneill, L.C., 2013. A method for semi-automated objective quantification of linear bedforms from multi-scale digital elevation models. Earth Surf. Process. Landf. 38, 221–236. https://doi.org/10.1002/esp.3269.

Daynac, J., Bessin, P., Shumack, S., 2024. A new workflow for mapping dune features (outline, crestline and defects) combining deep learning and skeletonization from DEM-derived data. Geomorphology 463, 1–15. https://doi.org/10.1016/j.geomorph.2024.109369.

Duffy, G.P., Hughes-Clarke, J.E., 2005. Application of spatial cross correlation to detection of migration of submarine sand dunes. Case Rep. Med. 110, 1–11. https://doi.org/10.1029/2004JF000192.

Gadhiraju, S.V., Shah, V., Buddhiraju, K.M., 2014. Segmentation of desert sand dunes. Remote Sens. Lett. 5, 961–970. https://doi.org/10.1080/2150704X.2014.980916.

Hayward, R.K.K., Fenton, L.K.K., Titus, T.N.N., 2014. Mars global digital dune database (MGD3): global dune distribution and wind pattern observations. Icarus 230, 38–46. https://doi.org/10.1016/J.ICARUS.2013.04.011.

Hood, D.R., Ewing, R.C., Roback, K.P., Runyon, K., Avouac, J.P., McEnroe, M., 2021. Inferring airflow across Martian dunes from ripple patterns and dynamics. Front. Earth Sci. 9, 1–17. https://doi.org/10.3389/feart.2021.702828.

Jackson, D.W.T., Bourke, M.C., Smyth, T.A.G., 2015. The dune effect on sand-transporting winds on Mars. Nat. Commun. 6, 1–5. https://doi.org/10.1038/ncomms9796.

Karabağ, C., Verhoeven, J., Miller, N.R., Reyes-Aldasoro, C.C., 2019. Texture segmentation: an objective comparison between five traditional algorithms and a deep-learning U-net architecture. Appl. Sci. 9, 1–14. https://doi.org/10.3390/app9183900.

Lapotre, M.G.A., Ewing, R.C., Lamb, M.P., 2021. An evolving understanding of enigmatic large ripples on Mars. J. Geophys. Res. Planets 126, 1–8. https://doi.org/10.1029/2020JE006729.

Lebrec, U., Riera, R., Paumard, V., O'leary, M.J., Lang, S.C., 2022. Automatic mapping and characterisation of linear depositional bedforms: theory and application using bathymetry from the north west shelf of Australia. Remote Sens 14, 1–24. https://doi.org/10.3390/rs14020280.

Lorenz, R.D., 2020. Martian ripples making a splash. J. Geophys. Res. Planets 125, 12–15. https://doi.org/10.1029/2020JE006658.

MacQueen, J., 1967. Some methods for classification and analysis of multivariate observations. In: Proceedings of the Fifth Berkeley Symposium on Mathematical Statistics and Probability, pp. 281–297. https://doi.org/10.1007/s11665-016-2173-6.

Matheron, G., 1963. Principles of geostatistics. Econ. Geol. 58, 1246–1266.

McEwen, A.S., Eliason, E.M., Bergstrom, J.W., Bridges, N.T., Hansen, C.J., Delamere, W. A., Grant, J.A., Gulick, V.C., Herkenhoff, K.E., Keszthelyi, L., Kirk, R.L., Mellon, M.T., Squyres, S.W., Thomas, N., Weitz, C.M., 2007. Mars reconnaissance orbiter's high resolution imaging science experiment (HiRISE). J. Geophys. Res. 112, 1–40. https://doi.org/10.1029/2005JE002605.

Nagle-Mcnaughton, T., McClanahan, T., Scuderi, L., 2020. Planet: a neural network for detecting transverse aeolian ridges on mars. Remote Sens 12, 1–15. https://doi.org/10.3390/rs12213607.

Pye, K., Tsoar, H., 2009. Aeolian Sand and Sand Dunes.

Reineck, H.-E., Singh, I.B., 1980. Depositional Sedimentary Environments, Second ed. Springer-Verlag, Berlin, Heidelberg, New York.

Rietkerk, M., Bastiaansen, R., Banerjee, S., van de Koppel, J., Baudena, M., Doelman, A., 2021. Evasion of tipping in complex systems through spatial pattern formation. Science (80-.) 374, 1–9. https://doi.org/10.1126/science.abj0359.

Robert, A., Richards, K.S., 1988. On the modelling of sand bedforms using the semivariogram. Earth Surf. Process. Landf. 13, 459–473. https://doi.org/10.1002/esp.3290130510.

Ronneberger, O., Fischer, P., Brox, T., 2015. U-Net: convolutional networks for biomedical image segmentation. In: Navab, N., Hornegger, J., Wells, W.M., Frangi, A.F. (Eds.), Medical Image Computing and Computer-Assisted Intervention – MICCAI 2015. Springer International Publishing, Cham, pp. 234–241.

Rubanenko, L., Perez-Lopez, S., Schull, J., Lapotre, M.G.A., 2021. Automatic detection and segmentation of barchan dunes on Mars and earth using a convolutional neural network. IEEE J. Sel. Top. Appl. Earth Obs. Remote Sens. 14, 9364–9371. https://doi.org/10.1109/JSTARS.2021.3109900.

Rubanenko, L., Lapôtre, M.G.A., Ewing, R.C., Fenton, L.K., Gunn, A., 2022. A distinct ripple-formation regime on Mars revealed by the morphometrics of barchan dunes. Nat. Commun. 13, 1–7. https://doi.org/10.1038/s41467-022-34974-3.

Rubin, D.M., 2012. A unifying model for planform straightness of ripples and dunes in air and water. Earth-Sci. Rev. 113, 176–185. https://doi.org/10.1016/j.earscirev.2012.03.010.

Sharp, R.P., 1963. Wind Ripples, 71, pp. 617–636. https://doi.org/10.1086/626936.

Sherman, D.J., Zhang, P., Bae, J., Butler, R.J., Baas, A.C.W., 2024. Morphology of barchan dunes on earth and Mars: classification and scale-invariance. J. Geophys. Res. Planets 129, 1–18. https://doi.org/10.1029/2024JE008526.

Silvestro, S., Vaz, D.A., Fenton, L.K., Geissler, P.E., 2011. Active aeolian processes on Mars: a regional study in Arabia and Meridiani Terrae. Geophys. Res. Lett. 38, 2–7. https://doi.org/10.1029/2011GL048955.

Silvestro, S., Vaz, D.A., Yizhaq, H., Esposito, F., 2016. Dune-like dynamic of Martian Aeolian large ripples. Geophys. Res. Lett. 43, 8384–8389. https://doi.org/10.1002/2016GL070014.

Skarke, A., Trembanis, A.C., 2011. Parameterization of bedform morphology and defect density with fingerprint analysis techniques. Cont. Shelf Res. 31, 1688–1700. https://doi.org/10.1016/j.csr.2011.07.009.

Sullivan, R., Kok, J.F., Katra, I., Yizhaq, H., 2020. A broad continuum of aeolian impact ripple morphologies on Mars is enabled by low wind dynamic pressures. J. Geophys. Res. Planets 125, 1–39. https://doi.org/10.1029/2020JE006485.

Tang, Y., Wang, Z., Jiang, Y., Zhang, T., Yang, W., 2023. An auto-detection and classification algorithm for identification of sand dunes based on remote sensing images. Int. J. Appl. Earth Obs. Geoinf. 125, 103592. https://doi.org/10.1016/j.jag.2023.103592.

Tanner, W.F., 1967. Ripple Mark Indices and Their Uses. Sedimentology 9, 89–104. https://doi.org/10.1111/j.1365-3091.1967.tb01332.x.

Tarnita, C.E., 2024. Self-organization in spatial ecology. Curr. Biol. 34, R965–R970. https://doi.org/10.1016/j.cub.2024.09.032.

van Dijk, T.A.G.P., Lindenbergh, R.C., Egberts, P.J.P., 2008. Separating bathymetric data representing multiscale rhythmic bed forms: a geostatistical and spectral method compared. Case Rep. Med. 113, 1–16. https://doi.org/10.1029/2007JF000950.

Vaz, D.A., Silvestro, S., Sarmento, P.T.K., Cardinale, M., 2017. Migrating meter-scale bedforms on Martian dark dunes: are terrestrial aeolian ripples good analogues? Aeolian Res. 26, 101–116. https://doi.org/10.1016/j.aeolia.2016.08.003.

Vaz, D.A., Silvestro, S., Chojnacki, M., Silva, D.C.A., 2023. Constraining the mechanisms of aeolian bedform formation on Mars through a global morphometric survey. Earth Planet. Sci. Lett. 614, 1–9. https://doi.org/10.1016/j.epsl.2023.118196.

Wasson, R.J., Hyde, R., 1983. Factors determind desert dune type.pdf. Nature 304, 337–339.

Wynn, R.B., Masson, D.G., Bett, B.J., 2002. Hydrodynamic significance of variable ripple morphology across deep-water barchan dunes in the Faroe-Shetland Channel. Mar. Geol. 192, 309–319. https://doi.org/10.1016/S0025-3227(02)00561-3.

Yizhaq, H., Tholen, K., Saban, L., Swet, N., Lester, C., Silvestro, S., Rasmussen, K.R., Merrison, J.P., Iversen, J.J., Franzese, G., Kroy, K., Pähtz, T., Durán, O., Katra, I., 2024. Coevolving aerodynamic and impact ripples on earth. Nat. Geosci. 17, 1–11. https://doi.org/10.1038/s41561-023-01348-3.

Zheng, Z., Du, Shihong, Du, Shouji, Zhang, X., 2020. A multiscale approach to delineate dune-field landscape patches. Remote Sens. Environ. 237, 1–18. https://doi.org/10.1016/j.rse.2019.111591.

Zheng, Z., Yu, Jinsongdi, Zhang, X., Du, Shihong, 2024a. Development of a 30 m resolution global sand dune/sheet classification map (GSDS30) using multi-source remote sensing data. Remote Sens. Environ. 302, 1–21. https://doi.org/10.1016/j.rse.2023.113973.

Zheng, Z., Zhang, X., Li, J., Ali, E., Yu, J., Du, S., 2024b. Global perspectives on sand dune patterns: scale-adaptable classification using Landsat imagery and deep learning strategies. ISPRS J. Photogramm. Remote Sens. 218, 781–801. https://doi.org/10.1016/j.isprsjprs.2024.10.002.